

Observation of Electron Bernstein Wave Heating in the RFP

A. H. Seltzman^{1*}, J. K. Anderson¹, S. J. Diem², J. A. Goetz¹, C. B. Forest¹

¹*Department of Physics, University of Wisconsin – Madison, Madison, WI, 53706, USA*

²*Oak Ridge National Laboratory, Oak Ridge 37831, Tennessee, USA*

(Received dd month 2017; published dd month 2017)

The first observation of rf heating in a reversed field pinch (RFP) using the electron Bernstein wave (EBW) has been demonstrated on Madison Symmetric Torus (MST). Propagation across and heating in a stochastic magnetic field has been observed. Novel techniques were required to measure the suprathermal electron tail generated by EBW heating in the presence of intense Ohmic heating. RF-heated electrons directly probe the edge transport properties in the RFP; measured loss rates imply a large non-collisional radial diffusivity.

DOI:

PACS numbers:

The Electron Bernstein wave (EBW) presents an alternative for heating and current drive in overdense plasmas where conventional extraordinary (X-mode) and ordinary (O-mode) electromagnetic waves do not propagate past the periphery. The EBW is a short wavelength electrostatic wave excited by mode conversion of externally launched electromagnetic (O or X) modes [1,2]. There are three distinct conversion schemes that have successfully driven EBWs in toroidal plasma configurations. In the first case, a launched O-mode couples to the X mode at the O wave cutoff layer and then the X mode converts to the Bernstein mode with near 100% efficiency at the upper hybrid layer. This OXB scheme has been used to heat [3] and drive current [4] in stellarator plasmas, and heat tokamak [5] plasmas. Second, a high-field side X mode launch converted to Bernstein mode has also been shown to heat [6] and drive current [7] in the conventional tokamak. A third scheme has been utilized to accommodate the high beta plasma of the spherical tokamak (ST) by low field side launch of the X mode. In this case, the X mode must tunnel through a narrow evanescent region before conversion to the Bernstein mode with efficiency near 100% [8] for optimal edge density gradient scale length, $L_n = n_e (dn_e/dx)^{-1}$, where n_e is the electron density; heating of the ST plasma [9] has been observed.

There are several factors that motivate continued study of the EBW in varied magnetic geometries. EBW finds use in component test facilities conducting first wall material studies for next-step fusion devices [10]. In advanced stellarators, EBW allows accessibility of the core to rf heating in high density. EBW propagation across a stochastic magnetic field is encouraging for both advanced tokamak heating scenarios (where resonant magnetic perturbations generate edge stochastic fields for edge localized mode control [11]) and the ST (where EBW may be utilized for current drive handoff after helicity injection startup). EBWs may be used to probe local beta limit and electron thermal gradient (ETG) stability in the reversed-field pinch (RFP) by localized heating in the well confined region of the strong temperature gradient at the edge.

The RFP presents a unique set of challenges to rf heating. The confining magnetic field is generated almost

entirely from current within the plasma, resulting in a large Ohmic heat input and a dynamic equilibrium with $|B|$ maximized on the magnetic axis (no high field side exists). The shape of $B(r)$ profiles is nearly fixed through the relaxation process that generates the equilibrium [12], with magnitude proportional to the plasma current. Current driven instabilities lead to strong edge density fluctuations that can diminish coupling efficiency to the EBW using OXB conversion [13]. Multiple internal resonant modes lead to a stochastic magnetic field over much of the plasma minor radius. A close-fitting conducting shell or an actively controlled saddle-coil system is required for stabilization of ideal external modes. The relatively weak magnetic field of the configuration leads to very overdense plasma ($\omega_p/\Omega_c > 5$, where ω_p is the plasma frequency and Ω_c is the cyclotron frequency). Inductive current profile control reduces tearing fluctuations generating high beta plasmas of $\beta=10-25\%$ [14], where beta is the ratio of plasma pressure to magnetic pressure. It should be noted that tearing, while a cause of the magnetic field perturbation, does not greatly affect the EBW process; large bursts of tearing activity are experimentally avoided. The $m=0$ (poloidally symmetric edge resonant) island is known to affect edge density and therefore mode conversion efficiency. In the discharges studied herein, the $m=0$ is of modest amplitude and tends to rotate at 4-5kHz, sweeping its phase around the machine on a time short compared to the rf pulse.

Previous studies of EBW physics in the RFP show efficient coupling, both through reciprocity in a blackbody emission measurement [15] and directly with optimization of a waveguide grill launching structure [16]. Ray tracing studies [17] predict accessibility of EBW heating and current drive over the outer half of the minor radius in Madison Symmetric Torus (MST) [18]. Full wave calculations of OXB mode conversion identify a feasible heating scenario in the RFX-Mod device considering realistic edge density fluctuations [19].

In this Letter, we report the first rf heating in the RFP configuration. Generation of a suprathermal electron tail during EBW injection in MST is measured in the presence of a Maxwellian background. Efficient mode conversion of an outboard-launched X mode wave at 5.5

GHz leads to Doppler-shifted resonant absorption, as shown in Figure 1 for a current yielding maximum accessible depth on the $n=2$ harmonic. In this diagram, the edge launched X-mode wave tunnels through the forbidden region between the right and upper hybrid locations, and mode converts into the Bernstein wave that propagates inward until absorbed. The Bernstein wave is strongly damped on a broad range of Doppler shifted cyclotron harmonics ($\omega_{rf} = n\omega_{ce} - k_{\parallel}v_{\parallel}$), where n is the harmonic number, as shown in Figure 5 for $n=1-5$. Experimental measurements show that the EBW propagates inward through a stochastic magnetic field to a minimum radius of $r/a \sim 0.8$, where $a=0.52\text{m}$ is the minor radius of MST and r is the EBW deposition radius, with the radial accessibility in MST limited by porthole-induced magnetic field error. In addition, the EBW-heated test electrons are used as a probe of edge ($r/a > 0.9$) radial transport, showing a modest transition from ‘standard’ to reduced-tearing RFP operation.

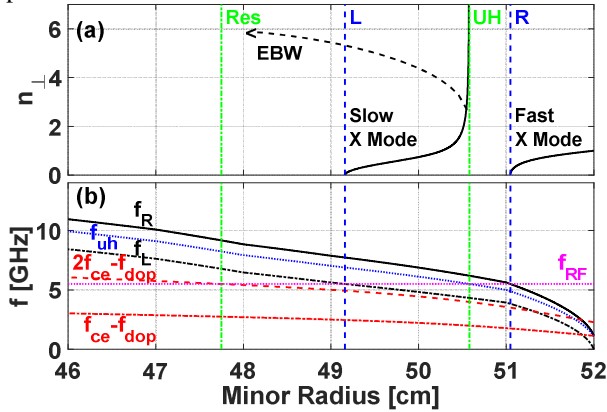


Figure 1. Plotted in (a) are index of refraction calculated for the X-mode wave (solid black), an illustrative curve for EBW (dashed black), and locations of the left (L) and right (R) cutoffs (dashed blue), upper hybrid (UH) resonance and Doppler shifted cyclotron resonance (Res) (dashed green). Plotted in (b) are the plasma frequencies, first and second harmonic Doppler shifted frequencies for 5.5GHz (f_{RF}) X-mode edge launch in a 210kA plasma. (color online)

Power from a 5.5GHz CPI VKC-7762B klystron was coupled to the fast X-mode by a 44.5mm ID cylindrical molybdenum antenna inserted flush to the inner wall. RF power was stabilized by feedback control. No local limiters or antenna aperture caps were used to alter edge density gradient. Sensitive fast electron diagnostics, and reduction of antenna porthole diameter proved imperative in demonstrating EBW heating.

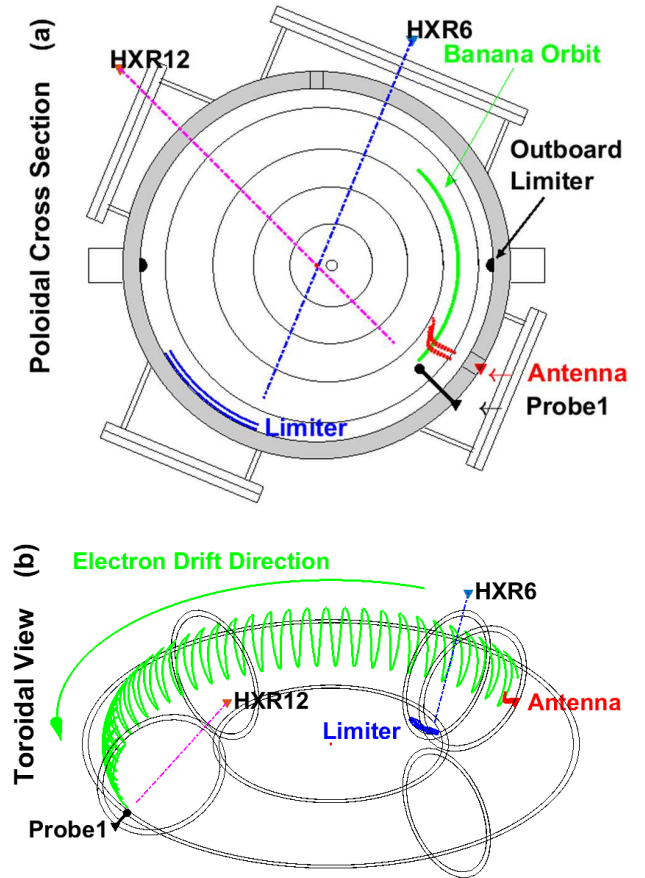


Figure 2. Poloidal cross section (a) of MST with poloidal field contours (black), computed EBW trajectory @138° Toroidal (red dots), banana orbit of heated electrons (green), limiter @150° Toroidal (blue solid line) and target probe Probe1 @300° Toroidal (black line) observed by HXR detectors HXR6 and HXR12, respectively. Toroidal view (b) of probe locations and trapped electron orbit (green). (color online)

A spatial distribution of solid targets with diametrically opposed x-ray detectors measures the dynamics of EBW-heated electrons. Target bremsstrahlung from the array of insertable molybdenum-tipped probes and fixed limiters is measured by energy resolved single photon counting HXR detectors [20] as shown in Figure 2. A target probe (Figure 2) is positioned at a toroidally-displaced location from the launch antenna. A typical EBW ray path, predicted in the ray tracing code GENRAY [21], is plotted in red in Figure 2. The ray has nearly zero toroidal propagation and the vertical deflection is an effect of toroidicity [17]. The actual beam trajectory is likely to be broadened by the imperfect magnetic field, and the finite extent of the antenna. While predominantly driving cyclotron motion, the large EBW k_{\parallel} upshift [17] and absence of a high toroidal field side trap only a modest fraction of heated electrons. Trapped and passing electrons both play an important role in the heated distribution. An inboard limiter displaced 12° toroidally from launch

(shown in blue in Figure 2) is used as a key diagnostic of electrons on passing orbits at the last closed flux surface (LCFS). An example trapped orbit (green) is plotted in Figure 2. As ∇B is in the minor radial direction (no high field side) trapped electrons experience a steady and rapid toroidal drift and zero banana width in the R-Z plane. Careful consideration of shadowing of the 1.27 cm outboard limiter (shown in Figure 2 (a)) on downstream measurements is required to properly analyze EBW deposition location.

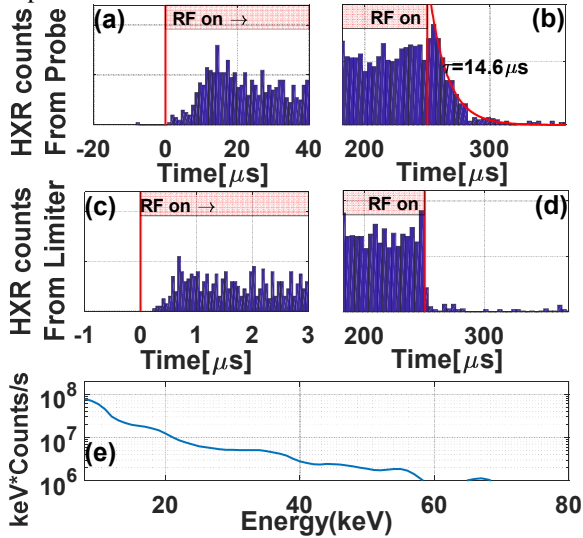


Figure 3. EBW induced x-ray measurements using a target probe inserted 3 cm from the wall in a 175 kA plasma. HXR rise time from probe (a) and limiter (c) is shown following the start of the pulse (note different timescale). HXR fall time from probe (b) and limiter (d) following rf pulse end. Time axis is with respect to pulse start. (e) HXR spectrum from target probe is shown averaged over pulse period. (color online)

EBW heating produces a clear supra-thermal electron tail in MST (even with an imperceptible change in stored energy in modest power experiments). Measured background flux from the non-rf heated discharge prior to rf turn-on in Figure 3(a) is negligible; for these plasma conditions the x-ray flux is generated entirely from the EBW-heated electrons. The typical x-ray spectrum is shown in Figure 3(e) with measurable flux between the 5 keV detector noise floor to 80 keV. For this study, a modulated rf pulse (2 kHz at 50% duty cycle) at ~30 kW net power (launched minus reflected) is injected into many reproducible 175kA RFP discharges. Experimentally this occurs during a window between 16-19 ms into the MST discharge during steady plasma current and line-averaged electron density. The line-averaged density is roughly $7 \times 10^{18} \text{ m}^{-3}$, core electron temperature ~150 eV and parameters at the upper hybrid layer are $n_e \sim 2 \times 10^{17} \text{ m}^{-3}$ and $T_e \sim 10 \text{ eV}$. Efficient coupling of 60-70% (inferred from measured reflected power) occurs without any antenna-specific limiter as the typical edge density gradient scale length ($L_n \sim 0.5\text{-}2 \text{ cm}$) is in a range favorable to X-B mode

conversion [16] in the antenna near field ($k_0 L_n \sim 1$ where k_0 is the vacuum wavenumber). Deposition is on the $n=3$ harmonic at an expected radial depth of 2.5 cm from the wall.

The difference in post-rf x-ray flux decay timescales between the probe (b) and limiter (d) in Figure 3 can be explained in terms of passing and trapped electrons and implies heating in a stochastic magnetic field [22]. The radial diffusion rate is proportional to the parallel velocity in a stochastic field; in MST this is a factor of $\sim 10^3$ greater for the passing electrons than for trapped electrons. Emission from the inboard limiter, 12° toroidally from the antenna, is determined by passing electron; much more common than deeply trapped electrons. Conversely, passing particles require several confinement times to reach the probe located $\sim 162^\circ$ toroidally away; probe emission is dominated by electrons on trapped orbits. Average measures of energy-integrated x-ray flux (HXR) from the probe are plotted for the rising, Figure 3(a), and falling, Figure 3(b), edges of the rf pulse. Following rf turn-off a characteristic decay of flux is used to infer a crude fast electron confinement time. Trapped fast electron confinement time in standard plasmas was 14.6 μs , as shown in Figure 3(b). Radial diffusion in the RFP controls electron loss; collisional times with background particles are on the order of one millisecond. Measured HXR rate decay time constant of $\sim 20\text{-}100 \text{ ns}$ on the inboard limiter shown in Figure 3(d) implies rapid loss of passing fast electrons. EBW heating experiments were conducted in reduced stochasticity (by inductive current profile control [14]) and an accompanying reduction in electron transport [23] with total β of 15-20%. While qualitatively similar to data in Figure 3, there is a factor of 3-5 increase in the EBW heated electron characteristic decay time [24], consistent with the drop in magnetic perturbations [25]. Falloff time constants between 2 cm and 8 cm depth varied from 12 μs to 34 μs , respectively, in standard plasmas, and 60 μs to 86 μs in reduced stochasticity plasmas.

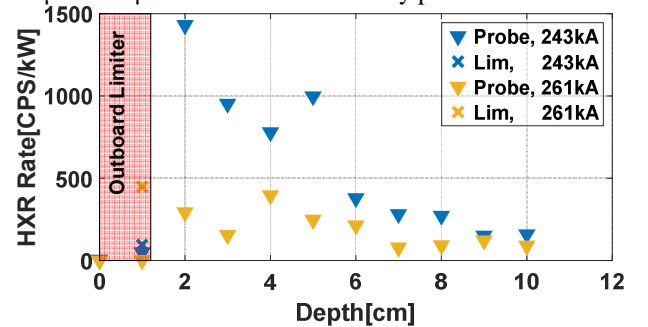


Figure 4. Radial profile of fast electron population from 0-10cm for select plasma currents measured with a target probe (\blacktriangledown) and limiter (X). Probe positions outside the LCFS are shadowed by the outboard midplane limiter, and measure negligible fast electron population. (color online)

Radial deposition of the EBW is measured from HXR flux from an insertable probe scanned from a depth of

0 cm (even with the wall) to 10 cm in a series of reproducible discharges. Examples at two plasma currents are shown in Figure 4, where a modest change in deposition center, $\langle r \rangle = \sum r\epsilon / \sum \epsilon$, where ϵ is HXR emissivity and r is measurement radius, is expected from the varied field strength. The flux is plotted versus probe position (\blacktriangledown , color keyed to plasma current). Note that in both plasma current cases, the emission is zero with the insertable probe tip in the shadow of the outboard limiter (depth < 1.25 cm). To accurately reconstruct the deposition profile, a measure of limiter emission is included (as an X plot symbol). These two examples give a deposition center of 3.8 cm and 2.3 cm at $I_p=240$ kA and 260kA, respectively. The large width of the deposition is likely caused by the substantial radial diffusion of electrons in the RFP edge [26].

Although the differences in the two deposition centers plotted in Figure 4 are subtle, repeating the measurement on a series of plasma currents yields a very clear trend. In Figure 5(a) the measured absorption center is plotted in green symbols as a function of plasma current ($I_p=200-270$ kA where $n=2$ resonant absorption is expected). The trend of deeper wave penetration with decreasing plasma current is both measured and expected. The expected deposition curve for the $n=2$ harmonic (solid blue line) is computed from the equilibrium magnetic field strength which gives the electron cyclotron resonance location for a frequency of 5.5 GHz, with corrections for porthole-induced field error and a substantial Doppler shift (details on each below). The quantitative agreement is confirmation of wave propagation across the stochastic edge of the tearing-dominated RFP discharge. The trend of increasing deposition depth halts at $I_p=205$ kA, where introduction of the $n=3$ harmonic at the wall begins to shift absorption to the edge.

The ability to resonantly deposit the EBW on several harmonics is clearly demonstrated by a measure of limiter emission over a large scan of plasma current. The equilibrium is similar for each discharge in the scan, making the plasma current axis equivalent to edge magnetic field strength. Figure 5(b) shows (in blue symbols) the power-normalized HXR emission from a limiter located 12 degrees toroidally from the launch antenna. Data points were filtered to remove points outside 3 standard deviations of a sliding window. Distinct peaks and troughs in intensity occur at particular values of plasma current. Limiter emission is measurable when the EBW is damped 1.5-3 cm from the wall and maximized for a depth of absorption of 2.5 cm. Only harmonics $n=1-5$ are plotted as a matter of clarity; measurements extending the plasma current from 50 to 550 kA show resonant absorption peaks for $n=1$ through 7. When the EBW deposition is more than ~ 3 cm from the wall, no edge emission is observed. The driving electromagnetic wave (incident from the depth=0 region) propagates inward for ~ 1 cm before encountering the right hand cutoff, shown in Figure 1(a). Conversion to the

Bernstein wave occurs at the upper hybrid layer, whose position is estimated by Langmuir probe measurements and plotted in red in Figure 5(a).

Bright limiter emission is evidence of strong edge damping of the Bernstein wave on each harmonic. Nulls in limiter emission indicate windows of substantial radial accessibility for each harmonic. Insertable probe measurements of deposition on the $n=2$ harmonic show maximum radial deposition in a region nearly free of limiter emission. The predicted deposition locations, plotted in blue in Figure 5 (a), are the Doppler-shifted cyclotron resonance after correction for porthole field error. The Doppler shift is calculated in GENRAY for a launched wave centered on $n_{||}=0$ that upshifts to -3 to -6 before absorption on electrons with $E_{||} = 50$ eV to 175 eV. Magnetic field error introduced by the interruption of the current carrying shell by the antenna porthole leads to a substantial reduction of field (up to 50%) at the wall[27], with the perturbation decreasing to zero radially inward at a diameter of the porthole. The main effect of porthole field error is the reduction in radial accessibility due to the introduction of a higher harmonic resonance at the boundary. In the absence of this field error, the radial accessibility of deposition on the $n=2$ harmonic would be ~ 10 cm at a plasma current of 165 kA. Due to field error contributions, the deepest deposition measured is 5 cm from the edge on the $n=2$ harmonic. The maximum accessibility in MST is therefore 10-12 cm from the edge for $n=1$ absorption at $I_p \sim 330$ kA. A direct measurement is not presented as the deeper radial location and higher plasma current conditions are not conducive to external probing.

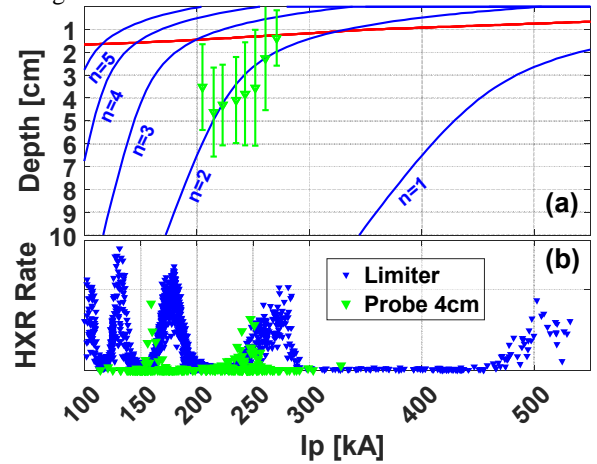


Figure 5. (a) Doppler shifted resonance location with porthole field error (blue) for harmonics ($n=1-5$) matches measured first moment of $n=2$ deposition (green \blacktriangledown). EBW mode conversion occurs at the UH layer (red). (b) HXR emission from the inboard limiter (blue) is maximized for deposition just inside the LCFS. Low limiter emission occurs when deposition is deeper than 3cm. Peak emission from a target probe 4 cm from the wall occurs at lower I_p than peak from limiter due to increasing deposition depth. (color online)

In summary, the first observation of RF heating in the RFP using the EBW is reported for fundamental and higher harmonics ($n=1-7$) utilizing XB mode conversion in the near field of a waveguide antenna. Propagation across, and heating in, regions of magnetic stochasticity are demonstrated. Deposition location was controllable with $|B|$. In the thick-shelled MST RFP, the radial accessibility of EBW is limited to $r/a > 0.8$ (~ 10 cm) by antenna porthole induced magnetic field error; accessibility in a thin-shelled device with actively controlled saddle coils (without substantial porthole field error) is likely to be $r/a > 0.5$ in agreement with ray tracing studies. Data in this paper is available online in digital format [28].

The authors would like to thank Brett Chapman and Karsten McCollam for their contributions to low I_p operation of MST, and Abdulgader Almagri for his contributions to probe setup and operation. This material is based upon work supported by the U.S. Department of Energy Office of Science, Office of Fusion Energy Sciences program under Award Number DE-FC02-05ER54814.

-
- [1] J. Preinhaelter, V. Kopecky, J. Plasma Physics. 10, 1 (1973)
 - [2] H. Sugai, Phys. Rev. Lett. 47, 1899 (1981)
 - [3] H. P. Laqua, et al. Phys. Rev. Lett. 78, 3467 (1997)
 - [4] H. P. Laqua, et al. Phys. Rev. Lett. 90, 075003 (2003)
 - [5] A. Mueck, et al. Phys. Rev. Lett. 98, 175004 (2007)
 - [6] T. Maekawa, et al. Phys. Rev. Lett. 86, 3783 (2001)
 - [7] V. Shevchenko, et al. Phys. Rev. Lett. 89, 265005 (2002)
 - [8] A. K. Ram, S. D. Schultz Phys. Of Plas. 7, 4084 (2000)
 - [9] S. Shiraiwa, et al. Phys. Rev. Lett. 96, 185003 (2006)
 - [10] J. Rapp, et al. IEEE Trans. on Plas. Sci. 44, 12, 3456 (2016)
 - [11] T.E. Evans, et al. J. Nuc. Materials. 337, 691-696 (2005)
 - [12] J. B. Taylor. Phys. Rev. Lett. 33, 1139 (1974)
 - [13] R. Bilato, F. Volpe et al, Nuc. Fusion. 49, 075020 (2009)
 - [14] B.E. Chapman, et al. Phys. Plasmas 9, 2061 (2002)
 - [15] P.K. Chattopadhyay, et al. Phys. Plasmas 9, 752 (2002)
 - [16] M. Cengher, J.K. Anderson, V. Svidzinski, C.B. Forest. Nuc. Fusion. 46, 521, (2006)
 - [17] C.B. Forest, P.K. Chattopadhyay, R.W. Harvey, and A.P. Smirnov, Phys. Plasmas 7, 1352 (2000)
 - [18] R.N. Dexter, et al. Fus. Sci. and Tech. 19, 131 (1991)
 - [19] R. Bilato, et al. Nuc. Fusion. 49, 075020 (2009)
 - [20] A. H. Seltzman, J. K. Anderson, A. M. DuBois, A. Almagri, and C. B. Forest. Rev. Sci. Instrum. 87, 11E329 (2016)
 - [21] A. P. Smirnov and R. W. Harvey, Bull. Am. Phys. Soc. 40, 1837 (1995)
 - [22] A. B. Rechester, M. N. Rosenbluth. Phys. Rev. Lett. 40, 38 (1978)
 - [23] R. O'Connell, et al. Phys. Rev. Lett. 91, 045002-1 (2003)
 - [24] A. Seltzman, Ph.D. Thesis, University of Wisconsin (2017)
 - [25] M. R. Stoneking, N. E. Lanier, S. C. Prager, J. S. Sarff, and D. Sinityn. Phys. Plasmas 4, 1632 (1997)
 - [26] T. D. Rempel, et al. Phys. Rev. Lett. 67, 1438 (1991)
 - [27] P. J. Fimognari, et al. Plasma. Phys. Cont. Fusion. 52, 095002 (2010)
 - [28] See supplementary material at [\[LINK HERE\]](#) for the digital format of data shown in this paper.